Journal of Materials Processing Tech. 299 (2022) 117316

Contents lists available at ScienceDirect

Journal of Materials Processing Tech.

journal homepage: www.elsevier.com/locate/jmatprotec

Validated dimensionless scaling law for melt pool width in laser powder bed fusion

Yangyiwei Yang [a], Alexander Großmann [b,*], Patrick Kühn [a], Jan Mölleney [b], Lorenz Kropholler [b], Christian Mittelstedt [b], Bai-Xiang Xu [a]

[a] Mechanics of Functional Materials Division, Institute of Materials Science, Technische Universität Darmstadt, Darmstadt 64287, Germany
[b] Institute for Lightweight Construction and Design, Technische Universität Darmstadt, Darmstadt 64287, Germany

ARTICLE INFO

Associate Editor: Adam Thomas Clare

Keywords:
Additive manufacturing
Laser
Powder bed fusion
Melt pool control
Scaling laws

ABSTRACT

The melting process during laser powder bed fusion (LPBF) is accompanied by complex physical phenomena, which can be rarely scaled with acceptable effort to utilize the melting process in component design to obtain tailored mechanical properties with adequate machine productivity. A constitutive law relating melt pool geometry to the process parameters thereby plays an essential role in practically fostering machine productivity and component quality in LPBF. In this work, we derive an improved dimensionless scaling law based on dimensional analysis to characterize the melt pool width, which is also capable of scaling the beam-size-dependent laser attenuation. Measurements from LPBF-produced specimens and 3D phenomenological LPBF finite element simulations are also performed in batch to validate the derived law. The regression analysis presents the correlation ∼97–98% for the simulated melt pool widths and ∼70–90% for experimental measured ones, with fabricated minimum strut thickness of 113 μm. After scaling the effective laser power with the calibrated laser attenuation, the proposed scaling law can be extended to be beam-size independent, as demonstrated by the regression of overall experimental measurements and simulation results, performed under different laser beam diameter, to the unified law with correlation $\geq$ 97%. It demonstrates the feasibility of proposed scaling law in melt pool controlled LPBF manufacturing for designing and producing thin-walled components with strut thicknesses in the micrometer range.

1. Introduction

Laser powder bed fusion (LPBF) is one of the most popular additive manufacturing (AM) technologies, bringing potentials to revolutionize component series production enabling innovation in the design of bionic lightweight products, as stressed in recent reviews by Panwisawas et al. (2020) and Velasco-Hogan et al. (2018). Smil (2013) also indicated that the development and application of LPBF contribute significantly to the reduction of material consumption as well as the carbon emission, and enable longer product life cycles in series components. Additionally, AM can engender unprecedented precision in fabricating nanoscale components such as micro-lattice structures. Notably, Meza et al. (2014) has achieved the manufacturing of the lattice metamaterials, composed of nanoscale ceramics, with simultaneously ultralight, strong, and energy-absorbing. Demonstrated micro-lattice also presents the capability of shape recovering.

Within the fabrication of metallic components, most of these depicted potentials remain still untapped due to the scarce consideration regarding effects from the manufacturing process, including exposure strategy and process parameters, on the continuous production of the components. The manufacturing process is known to have a considerable influence on the economical fabrication as well as technical aspects, including the component's porosity (Bauereiß et al., 2014), microstructure (Herzog et al., 2016), anisotropy (Popovich et al., 2017), particle adhesion, and residual stresses (Robinson et al., 2018). The ongoing development in novel LPBF machines and powder alloys complicates the inclusion of the fabrication process into the design of economically competitive components with tailored properties. All of the aforementioned properties are influenced by the thermo-mechanical behavior and geometry of the melt pool, which makes it crucial to find suitable methods to characterize both the geometry and underlying physical behavior to enable melt pool controlled LPBF.

Identifying and understanding the underlying physics during LPBF and their interplay enable the parameterized exploration for the melt

* Corresponding author.
E-mail address: alexander.grossmann@klub.tu-darmstadt.de (A. Großmann).

https://doi.org/10.1016/j.jmatprotec.2021.117316
Received 20 May 2021; Received in revised form 29 July 2021; Accepted 1 August 2021
Available online 4 August 2021

pool control, and eventually reduce the aforementioned market entry barriers of LPBF. Emphasized by King et al. (2015), predicting and controlling the melt pool geometry directly bridge the gap between the process parameters and the resultant microstructure and properties. Various approaches have been carried out for modeling and simulation of LPBF processes, as adequately reviewed by King et al. (2015) and Markl and Körner (2016), demonstrating its instructive role in recognizing and regulating the melt pool phenomena and geometry. Curtarolo et al. (2013) also depicted the contributions from the LPBF simulations to the state-of-art computational approaches such as high-throughput and data-driven computing, where a colossal database containing calculated characteristic properties of both existent and predicted materials can be created for searching, screening, and optimizing desired performances intelligently and automatically.

Markl and Körner (2016) have summarized characteristic physical effects during LPBF, commenting that these underlying phenomena cover broad time and length scales with various origins. Employing In-situ X-ray imaging, Leung et al. (2018) unveiled the complex nature of the melt pool dynamics, driven by the interaction among incident laser rays as well as solid, melt, and vapor at speeds ranging from hundreds to thousands of meters per second. These features were also elucidated in the combined high-speed and schlieren imaging by Bidare et al. (2018) and the state-of-art high-fidelity melt pool dynamics simulation by Khairallah et al. (2020). As a result, the thermal transfers and material transformations, notably the heat conduction and radiation, melting and solidification, and evaporation, dominate on a length scale of hundreds to thousands of micrometers over a few dozen milliseconds, comparing to the component fabrication taking hours or even days. Wang et al. (2018) has also demonstrated the resultant microstructure from a LPBF-processed 316L stainless steel in a multiscale fashion. On the other hand, due to the existence of high cooling rate and variation in morphologies, a locally concentrated high-gradient thermal profile can be expected, which leads to temperature-gradient-driven effects and further complexities. As derived by Yang et al. (2020) under a thermodynamic consistent framework, these temperature-gradient-driven effects should be spontaneously coupled with commonly considered physical processes, such as mass and heat transfer, and the melt pool dynamics. Remarkably, the thermocapillary effect, i.e., the surface tension gradient induced by the local inhomogeneity of temperature, is believed to be the primary driving force of the in-process Marangoni convection and Plateau-Rayleigh instability. Khairallah et al. (2016) has demonstrated the significant role of Marangoni convection in shaping the melt pool flow and resultant denudation, spattering, and pore defects in the manufactured component. Meanwhile, the wavy and unstable melt track attributes to the Plateau-Rayleigh instability. These phenomena were further identified and characterized by Guo et al. (2020) as the factors that could deteriorate the surface quality for the manufactured components.

Through the various spatio-temporal scales of the LPBF process, King et al. (2015) stressed the involvement of a large number of intrinsic and extrinsic parameters, showing the vast complexity in the sense of controlling the melt pool under consideration of multiple aspects. It illustrates the need to develop constitutive laws that describe these phenomena by means of closed-form analytical equations, which can find application in process development and optimization as well as the laser-driven design of thin-walled components. Denoting as the relative quantities with an absolute meaning (Bridgman, 1922), dimensionless numbers, based on the Buckingham (1914) Π-theorem, are utilized to reduce the complicity of the physics systems with interactive mechanisms and reveal the potential relations among physical quantities. This method has been applied successfully in fluid dynamics, biology (Purcell, 1977; West et al., 1997), biomechanics (Pelz and Vergé, 2014), nuclear physics (Barenblatt, 1996), and most recently in LPBF (Mukerjee et al., 2017; Rubenchik et al., 2018). Although it is an ongoing field to derive constitutive laws regarding melt pool control, there are notable works with defined dimensionless numbers, which deliver consistent and unified understandings regarding relations among melt pool geometries, material properties and process parameters. They are:

(1) The Peclet number (Pe), describing the ratio between convective and conductive heat transport, and as an important quantity to determine the size of the melt pool (Rai et al., 2007);
(2) The effective power (P_+), a dimensionless notation of the laser power that correlates with the Pe number and thus gives an information on the width of the melt pool (Großmann et al., 2019);
(3) The Marangoni number (Ma), denoting the ratio between surface tension based and viscous forces. Therefore, it describes the effectivity of heat distribution within the liquid melt pool and is positively correlated with the Pe number, signifying, that higher Ma numbers lead to larger melt pools (Mukerjee et al., 2017);
(4) The dimensionless enthalpy (H^*), indicating a ratio of specific energy absorbed by the material and the energy, which is necessary for melting and correlates with the melt pool depth (King et al., 2014).

As one of the widely-characterized geometric parameters, melt pool depth has been sufficiently investigated in the present literature. Previous researches from welding, notably by Rai et al. (2007) and Hann et al. (2011), have stressed the importance of calculating the melt pool depth to assess the process stability and the welding modes (surface mode vs. keyhole mode). This was later transferred towards LPBF by King et al. (2014) and Rubenchik et al. (2018) with a developed dimensionless framework to predict the both the melt pool depth and the melting mode. However, the depth is hardly inferable from the current monitoring systems and thus not feasible in the sense of melt pool control. Instead, melt pool width can be readily monitored and employed to determine the corresponding depth and present melting mode (conduction mode vs. keyhole mode as termed by Metelkova et al. (2018)). This procedure was shown by Goossens and van Hooreweder (2021), where the melt pool width is measured by a camera and the resulting depth calculated with a semi-analytical relation derived by Fabbro et al. (2018). This highlights the importance of developing reliable constitutive laws for melt pool width, which has rarely been presented in the recent additive manufacturing related literature.

Additional to the monitorability, melt pool width is with high interests in the fabrication of thin-walled cellular structures (including lattice or honeycomb structures) for the application of lightweight manufacturing, due to its determinant role on the homogenized mechanical property of the produced structures, as shown by Souza et al. (2018). Nonetheless, many relevant quantities (i.e., the process parameters and material properties) with high impact on the melt pool width are not included in the aforementioned works. To fill in this blank, allometric scaling laws have been proposed to relate Pe to P_+ by Großmann et al. (2019) for the single fusion track, which has been later extended for the case of two adjacent melt tracks (contour exposure) by Großmann et al. (2020) with the P_+ and two Peclet-type numbers, i.e., a Pe_d characterizing the resultant strut thickness, and a Pe_h characterizing the hatching distance (the distance between two adjacent scan tracks). Within the process window (PW) where the melt pool is formed regularly without pronounced Plateau-Rayleigh instability and keyholing (i.e., the conduction model), the proposed allometric scaling law has been validated to be material independent with various powder alloys, including stainless steel 316L (SS316L), nickel IN625, aluminum AlSi10Mg, AlMgSc, maraging steel MS1, and titanium Ti6Al4V, as all experimental measurements on various powder materials regress to the unified law. It also allows for inverse scaling of the precision and productivity for LPBF-processed component, as pointed out by Großmann et al. (2019). However, the proposed scaling law did not include the influence from the laser beam size, which also has significant effects on the resultant melt pool width. As stressed by Boley et al. (2017), the absorptivity of the powder bed can be sensitive to the laser beam size, as its increase can reduce the fluctuation in the local absorption of the

laser. The beam size, along with the specific laser power, should be also the determinant factors to the magnitude of the melting pool and associated laser ray behaviors. As visualized by high-fidelity simulation by Khairallah et al. (2020) with laser ray tracing, the beam size (with relatively low powder) directly related to the proportion of incident rays that interact with non-fused powders around the front of the melt pool, reflecting again the beam-size dependency of the powder bed absorptivity. From the perspective of application, the laser beam size is also closely related to the productivity of the LPBF process, enabling an increase of 840% along with a high energy input, as pointed out by Metelkova et al. (2018).

In this contribution, we extended this previously developed scaling law to be further beam-size independent. The paper is organized as follows: in Section 2 the fundamental concepts regarding dimensional analysis and the phenomenological modeling are given, with introducing a beam-size-dependent uncertainty $\eta(D_l)$, which is physically related to the laser penetration and calibrated from the the experimental measurements. Section 3 details the materials and methodsemployed in this work. In Section 4 the experimental and numerical results are visualized in both dimensional width–energy-density diagrams and dimensionless P_+-Pe diagrams. Here, an improved allometric scaling law that includes the beam diameter is derived and discussed from the aspects of regression analysis. In Section 5 the added value by this contribution combined with potential applications and a proposal for future directions of research are given.

2. Theory

2.1. Dimensional analysis

As stressed above, the melt pool width determines both the accuracy and the economical efficiency of the LPBF process. An allometric scaling law to characterize the melt pool geometry, i.e., $Y = CE^i$ with a geometry-related quantity Y, a process-dependent variable E and coefficient C as well as index i, is thus highly desirable yet absent in the available literature. Pointed out by Großmann et al. (2019), the melt pool width b correlates with the linear energy density $E_L = P/v$ in form of $b = CE_L^i$, where P and v are the laser power and scan speed. It is worth noting that this scaling law is valid within the PW, where the melt pool is formed with the conduction mode, as shown in Fig. 1a. To ensure comparability between different powder and machine types, which is a key enabler for the melt pool controlled LPBF, a dimensionless coefficient $\Lambda = D_l/d_{50}$ was also introduced by Oliveira et al. (2020), where D_l and d_{50} represent the laser beam diameter and the mean particle diameter. This leads to a new linear energy density formulation $E_L^* = \Lambda E_L$. Despite better comparability among different machines and powders by the coefficient Λ, the coefficient C and index i must still be determined for each machine and material set in order to compute the melt pool width. This emphasizes the need for dimensionless scaling laws.

In the previous work by Großmann et al. (2019), dimensional analysis was performed on the LPBF melting process. By employing the Buckingham Π-theorem on six quantities of interest, i.e., the melt pool width b, the laser power P, the scanning speed v, the heat conductivity k, the volumetric specific heat ρc, and the characteristic temperature difference $\Delta T = T_M - T_0$ with the melting temperature T_M and the substrate temperature T_0, and four fundamental dimensions, i.e., the length (L), the mass (M), the time (T) and the temperature (Θ), the whole system can be eventually described by two dimensionless numbers, i.e., a Peclet-type number Pe and the other newly-defined one, termed here as effective laser power P_+

$$\mathrm{Pe} = \frac{bv\rho c}{k}, \quad \mathrm{P_+} = \frac{Pv\rho c}{k^2\Delta T}, \tag{1}$$

each of which is also the combination of dimensional quantities. This allows us to scale the melt pool width in a dimensionless manner according to the allometric scaling function $\mathrm{Pe} = f(\mathrm{P_+})$. Based on the experimental observations by Großmann et al. (2019), it is further deduced that convection mechanism, rather than heat transfer, governs the energy flow in and out of the melt zone in LPBF. In this regard, the melting and resolidification process can be legitimately approximated to be adiabatic, which thereby cancels out the influences from heat conductivity k. In this regard, a single dimensionless parameter $\mathrm{H_{adi}}$ can be defined as

$$\mathrm{H_{adi}} = \frac{b^2 v\rho c\Delta T}{P}. \tag{2}$$

Detailed analysis is sufficiently summarized in Appendix B. According to its formulation, this $\mathrm{H_{adi}}$ clearly features an efficiency characterizing the ratio between absorbed energy to elevate the temperature ΔT of a transient finite volume $\dot{V} = b^2 v$ and the laser power P at the adiabatic condition. It thereby termed as "adiabatic energy efficiency" in this work. It is worth noting that this transient volume $\dot{V}$ can also adopt the meaning of the characterized melt pool volume by relating melt pool depth to the width proportionally, i.e., $d \propto b$, which can be also mathematically portrayed as the first-order approximation of the d, i.e., $d(b) = d_0 + d_1 b + o(b^2)$ with the coefficients d_0 and d_1 and the high-order infinitesimal $o(b^2)$. In works by Fabbro et al. (2018) and Goossens and van Hooreweder (2021), d and b are directly related by a proposed melt-pool depth-to-width ratio R.

Based on Eq. (2), a allometric relation between the melt pool width and the linear energy density can be formulated as follows,

$$b = C_L E_L^{0.5} \tag{3a}$$

with the corresponding coefficient $C_L = \mathrm{H_{adi}}\sqrt{1/\rho c\Delta T}$. One can also reformulate Eq. (3a) by introducing one volumetric energy density $E_V = I/v$ with the mean irradiance of the laser beam $I = 4P/(\pi D_l^2)$

$$b = C_V E_V^{0.5}, \tag{3b}$$

in which $C_V = \sqrt{\pi} C_L D_l/2$. Submitting Eqs. (1) and (2) to either the Eq. (3a) or Eq. (3b), the following scaling law among dimensionless numbers can be derived

$$\mathrm{Pe} = \mathrm{H_{adi}} \mathrm{P_+^{0.5}}. \tag{4}$$

As validated on various powder alloys by Großmann et al. (2019) and Großmann et al. (2020), the scaling laws $\mathrm{Pe} = 0.24\mathrm{P_+^{0.67}}$ and $\mathrm{Pe}_d = 0.96\mathrm{Pe}_h + 0.18\mathrm{P_+^{0.7}}$ were obtained based on fitting of the experimental measured resultant strut thickness b_d on various the hatch distance b_h, which were adopted as the characteristic lengths in computing the Peclet-type number Pe_d and Pe_h, respectively.

To further consider the influence from D_l with clear-portrayed physical foundations, a dependent uncertain parameter $\eta(D_l)$, adopting the physical meaning as the laser efficiency, should be introduced as stressed by Boley et al. (2017) that the laser absorptivity is sensitive to the laser beam size. Further stressed by Khairallah et al. (2020), it is no doubt that η can depend on further quantities like absorptivity, particle diameter, layer thickness and absolute layer height. Nonetheless, effects from those quantities are not included in this work. This is justifiable in the sense of a first-order approximation, where those quantities are assumed to have a minor influence on the scaling law. Besides, according to the objective of the dimensional analysis proposed by Buckingham (1914), it is desired to have a coarse-grained model with as few input parameters as possible, which can reliably predict the regarded physical system. The remaining question is how this beam-size-dependent laser efficiency get involved into the physical system. This requires the specific deduction from the perspective of physical modeling and calibration at the identical condition w.r.t. the experimental measurements, which will be explicitly covered in the coming

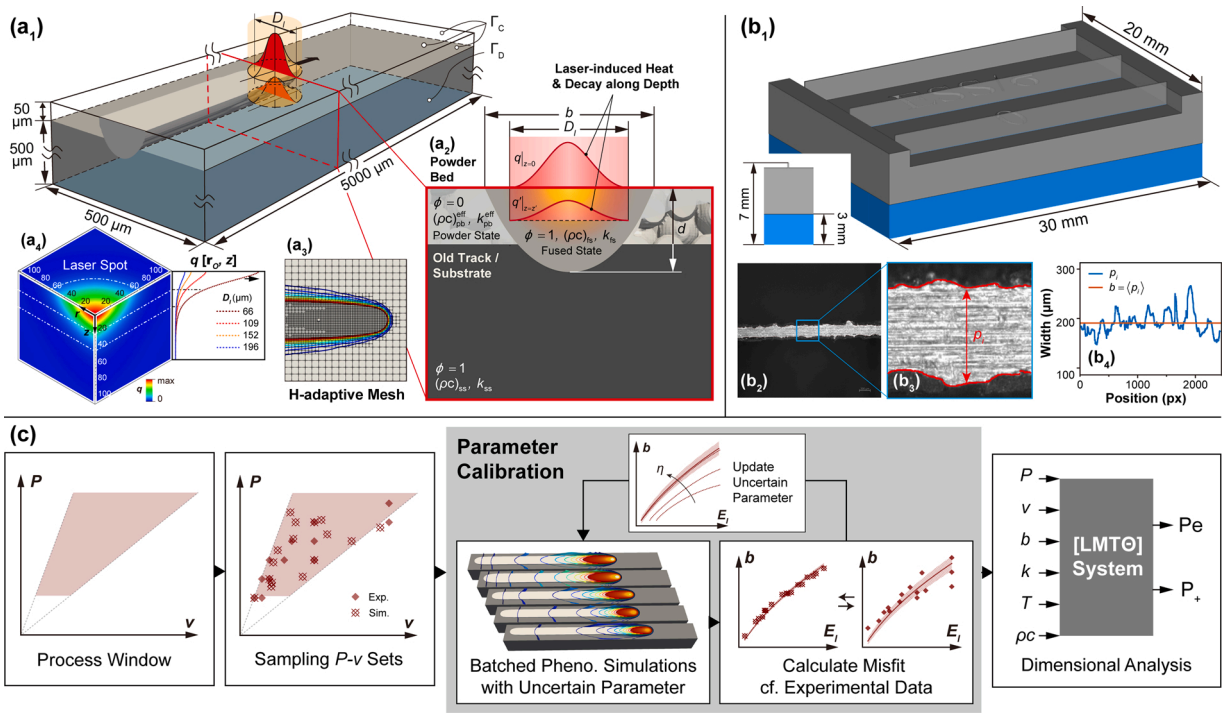

Fig. 1. (a) Schematic diagrams of the 3D phenomenological LPBF models. (b) Specimen geometry and pixelized visual analysis on processed components. (c) Workflow of phenomenological-simulation-assisted analysis scheme.

section.

2.2. Phenomenological LPBF model

In order to verify the proposed scaling law from the theoretical aspects, a 3D phenomenological LPBF transient model implemented for the simulations is thereby introduced. Following the concept proposed by Yi et al. (2019), one phenomenological field ϕ is introduced to indicate the fusion of the powder bed, i.e. $\phi = 1$ for the fused state (including old track/substrate) and $\phi = 0$ for the non-fused (powder) state, as shown in Fig. 1a$_2$. Then the governing equations of the transient thermal transfer and the powder bed fusion can be formulated as

$$\rho c(\phi, T)\frac{\mathrm{D}T}{\mathrm{D}t} = \nabla\cdot k(\phi, T)\nabla T + q, \tag{5}$$

$$\phi \xrightarrow{T\geq T_\mathrm{M}} 1, \tag{6}$$

where $\mathrm{D}(\cdot)/\mathrm{D}t = \dot{T} - \mathbf{v}\cdot\nabla T$ is the total derivative with the scan velocity $\mathbf{v}$. $\phi \xrightarrow{T\geq T_\mathrm{M}} 1$ represents the irreversible change of ϕ, which is initialized as zero in the powder bed layer, to one when the local T is once beyond the melting point T_M. The heat conductivity k and volumetric specific heat ρc take temporal-spatial distribution indicated by ϕ, i.e.

$$\begin{aligned} k(\phi, T) &= \phi k_\mathrm{fs}(T) + (1-\phi)k_\mathrm{pb}^\mathrm{eff} \\ \rho c(\phi, T) &= \phi(\rho c)_\mathrm{fs}(T) + (1-\phi)(\rho c)_\mathrm{pb}^\mathrm{eff} \end{aligned} \tag{7}$$

with

$$\begin{aligned} (\rho c)_\mathrm{fs} &= \begin{cases} (\rho c)_\mathrm{ss} & T < T_\mathrm{M} \\ (\rho c)_\mathrm{ss} + \dfrac{\partial \mathscr{L}}{\partial T} & T = T_\mathrm{M} \\ (\rho c)_\mathrm{ml} & T > T_\mathrm{M} \end{cases}, \\ k_\mathrm{fs} &= \begin{cases} k_\mathrm{ss} & T < T_\mathrm{M} \\ k_\mathrm{ml} & T \geq T_\mathrm{M} \end{cases}, \end{aligned} \tag{8}$$

where $\mathscr{L}$ represents the latent heat during melting. Effective thermal properties such as volumetric specific heat $(\rho c)_\mathrm{pb}^\mathrm{eff}$ and thermal conductivity $k_\mathrm{pb}^\mathrm{eff}$ of the powder bed, as well as the laser-induced heat rate q are characterized as the collective outcomes of material properties of the powder and atmosphere (thermal and optical), powder size distribution, beam-size-dependent parameters (e.g., D_l) and other distinct physical processes (convection, radiation, and laser–powder-bed interactions). These will be explicitly introduced in the following subsections.

2.2.1. Effective thermal properties of the powder bed

The effective specific heat of the powder bed $(\rho c)_\mathrm{pb}^\mathrm{eff}$ can be simply estimated according to the rule of mixtures in this work, i.e.

$$(\rho c)_\mathrm{pb}^\mathrm{eff} = \varphi(\rho c)_\mathrm{at} + (1-\varphi)(\rho c)_\mathrm{ss}, \tag{9}$$

where $(\rho c)_\mathrm{ss}$ and $(\rho c)_\mathrm{at}$ are together known as the volumetric specific heat of solid and atmosphere, respectively. φ is the porosity estimated from the characteristic diameters of the powder size distribution, i.e. d_{10}, d_{50} and d_{90}, based on statistics of the random packing simulations performed by Desmond and Weeks (2014) (summarized in Appendix A)

The effective thermal conductivity of the powder bed, however, remains debatable as multiple assumptions or simplifications regarding the powder bed structures have been made and suggested among various works. Some representative models of $k_\mathrm{pb}^\mathrm{eff}$ with featured structure, such as Voigt and Reuss model, Maxwell (1954) model, effective media theory (EMT) by Kirkpatrick (1973) and the Zehner-Schlünder-Sih (ZSS) model by Sih (1996) are summarized in Fig. 2a with insets presenting the schematic representations of the microstructure assumed by corresponding models.

Remarkably, there are two of the widely-employed models in the existent researches considering the homogenized powder bed. The Voigt model, reading as

$$\frac{k_\mathrm{pb}^\mathrm{eff}}{k_\mathrm{at}} = \left(1-\varphi\right)\frac{k_\mathrm{ss}}{k_\mathrm{at}} + \varphi, \tag{10}$$

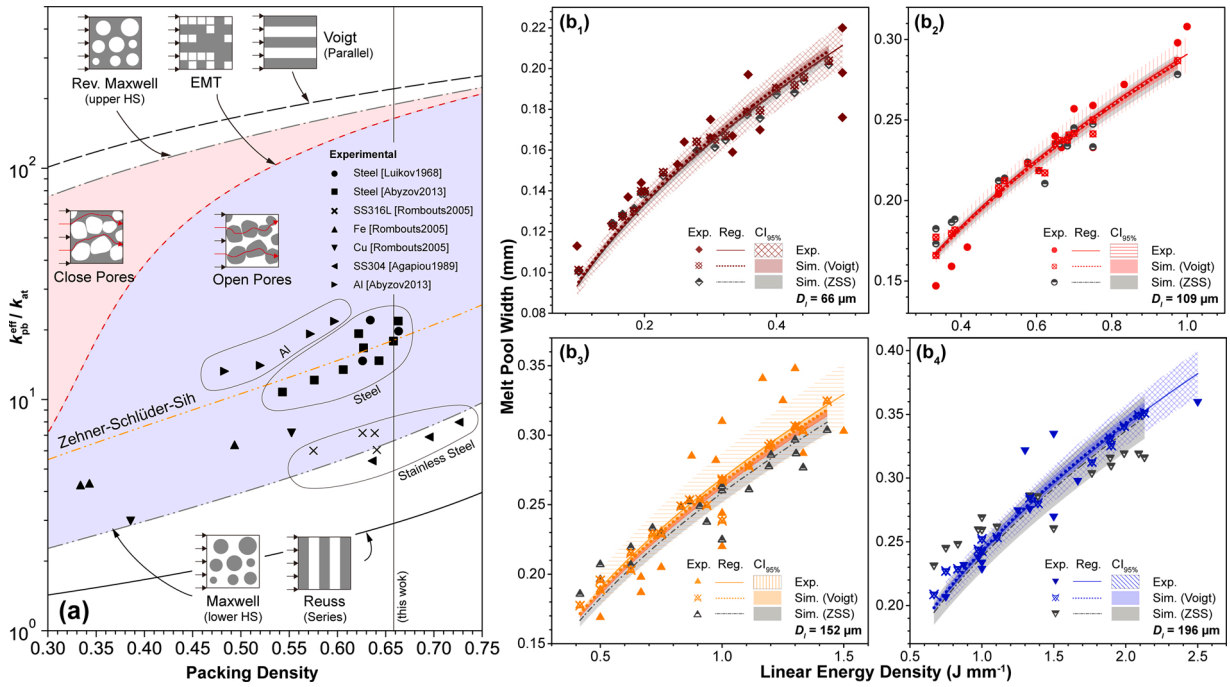

Fig. 2. (a) Effective heat conductivity of the powder bed vs. packing density obtained from distinct models and measurements of the free powders. (b_1)-(b_2) Comparison of the non-linear regression of $b = C_L E_L^{0.5}$ among experimental measurements and calibrated phenomenological simulations using Voigt model and ZSS model.

or simply $k_{pb}^{eff} = (1-\varphi)k_{ss}$ for negligible k_{at}, was suggested originally by Thümmler et al. (1993) from the perspective of powder metallurgy. It was then utilized by Hussein et al. (2013) and Li and Gu (2014) in simulating the local temperature profile and melt pool geometery, and most recently by Arısoy et al. (2019) who compared the simulation results with experimental thermal images on the LPBF-processed Inconel 625 powder bed. On the other hand, the ZSS model

$$\frac{k_{pb}^{eff}}{k_{at}} = \left(1-\sqrt{1-\varphi}\right) + \sqrt{1-\varphi}\left[\frac{2}{1-\frac{Bk_{at}}{k_{ss}}}K\right] \tag{11}$$

with

$$K = \frac{(1-\frac{k_{at}}{k_{ss}})B}{(1-\frac{Bk_{at}}{k_{ss}})^2}\ln(\frac{k_{at}}{Bk_{ss}}) - \frac{B+1}{2} - \frac{B-1}{1-\frac{Bk_{at}}{k_{ss}}},$$

$$B = 1.25\left(\frac{1-\varphi}{\varphi}\right)^{\frac{10}{9}}$$

was proposed by Sih (1996) with originally the consideration of contacting and radiation effects on powders with different geometry. It was then utilized by Romano et al. (2015) in comparing the local temperature profile as well as melt pool geometry in powder bed fusion among common materials, and later validated by Denlinger et al. (2016) with the *in situ* measurements on the LPBF-processed Inconel 718 powder bed. In this work, both Voigt and ZSS models are compared and discussed regarding regression analysis to the experimental measurements in order to examine their coherency in reflecting the relation between process parameters and melt pool width.

2.2.2. Laser-induced heat effect and absorptivity calibration

The thermal effect incited by laser is equivalently treated as a volumetric heat source with its distribution along the depth direction formulated in a radiation penetration fashion, as the powder bed is regarded as an effective homogenized optical medium. Considering a scanning laser on the surface with a velocity v and a power P, its induced heat rate q at any point $\mathbf{r}(x,y,z)$ (with $\mathbf{r}_S(x,y,0)$ representing its projection onto the surface) and any time t in the powder bed can be formulated as

$$q[\mathbf{r}(x,y,z),t] = Pp_{xy}[\mathbf{r}_S(x,y,0),t]\frac{\mathrm{d}a^{eff}}{\mathrm{d}z}, \tag{12}$$

in which the in-plane distribution p_{xy} is always taken 2D-Gaussian type if only consider the fundamental transverse electromagnetic mode (TEM_{00}) of the laser, as demonstrated by Roberts et al. (2009)

$$p_{xy}(\mathrm{r}_S,t) = \frac{4\Pi}{\pi D_l^2}\exp\left[-4\Pi\frac{\|\mathrm{r}_S - \mathbf{v}t\|^2}{D_l^2}\right] \tag{13}$$

with the nominal laser beam diameter D_l as well as a parameter Π to adjust the concentrated power within the spot. It is worth noting that there is no universal-accepted definition of laser diameter, yet Π's value should be strict to the selection of the D_l. For instance, Yang et al. has employed the full-width at half-maximum (FWHM) as D_l in simulating the selective laser sintering (Yang et al., 2019) and follow-up LPBF of SS316L (Yang et al., 2020), i.e., $\Pi = \ln 2$, implying 50% of the surface laser power is within the spot of D_l = FWHM. In this work we take the second moment width (or four times the standard deviation, $D_{4\Sigma}$) as D_l as suggested by ISO (2005) standard. In this case, $\Pi = 2$, indicating 86.5% of the concentrated power within the spot.

Direct measurements by Rubenchik et al. (2015) reveals that the powder materials as well as packing density can further affect the absorption rate of laser. King et al. (2015) has stressed that the effective absorptivity of laser a^{eff} is treated as one of the primary sources of uncertainty in the system, mainly due to its strong dependence on the local transient morphology. It also receives influences from the beam-size-dependent factors, such as laser wavelength and beam size (D_l). To confront this issue, the parameter $\eta(D_l)$, emphasizing the

potential laser attenuation due to the variation in D_l, is also considered in the phenomenological model as

$$\frac{\mathrm{d}a^{\mathrm{eff}}}{\mathrm{d}z} = -\eta(D_l)\overline{\beta}(d_{50},\varphi)\frac{\mathrm{d}Q}{\mathrm{d}\zeta}. \tag{14}$$

The mean attenuation coefficient $\overline{\beta}$ is formulated in this work as follows, assuming a loosely packed powder bed with the estimated porosity φ and the median diameter of the powder d_{50}

$$\overline{\beta} = \frac{3}{2}\frac{1-\varphi}{\varphi}\frac{1}{d_{50}}. \tag{15}$$

The optical path is then $\zeta = \overline{\beta}z$. The formulation of the dimensionless net radiative energy flux density $Q(\zeta)$ has been derived by Gusarov et al. (2009) for thin layers of metallic powders placed on a reflective substrate. Thermal effects on SS316L induced by $q[\mathbf{r},t]$ (shown in Fig. 1a$_4$) are also benchmarked numerically by Gusarov et al. (2009) and Yang et al. (2019), and experimentally by Khairallah and Anderson (2014).

Notably, Eq. (14) has introduced aforementioned beam-size-dependent laser efficiency η, which is calibrated inversely by nonlinear regression analysis w.r.t. the experimental measurements under different D_l. The workflow is shown in Fig. 1c comprehensively. To be brief, batched phenomenological simulations were performed within the identical PW of the experiments. The scaling law $b = C_L\sqrt{E_L}$ was herein adopted as the criterion to identify of the misfit of the simulation to the experimental results under the same D_l. The uncertain parameter η was thereby iterated until the misfit of the regression coefficient, i.e. C_L, is less than 1%.

3. Materials and methods

3.1. Machine and materials

The specimens were fabricated on a direct metal laser sintering machine EOS M 270 (EOS GmbH) with laser powers of 195–370 W, scan speeds 50–2000 mm s^{-1}, and laser beam diameters 66–196 μm. The laser diameters have been determined with a *ScanFieldMonitor* (PRIMES GmbH). The investigation has been conducted with the commercially available stainless steel alloy 316L with a particle size distribution $d_{10} = 16.12$, $d_{50} = 28.78$, and $d_{90} = 42.23\mu$m, determined through scanning electron microscopy using a *Phenom Pro X*.

3.2. Method of measurements

Single scan tracks have been printed with different process parameters using the specimen design shown in Fig. 1 b$_1$. The widths have been determined by processing microscope images of mattlack sprayed and polished top-view specimen in a self-written MATLAB code for digital image processing. Visual evaluation is then conducted to observe the polished micro-sections under the processing microscopic (Fig. 1b$_2$). Melt pool width b is then taken as the average of the measured distance p_i between two pixelized trajectories (Fig. 1b$_3$–b$_4$).

3.3. Numerical methods

The phenomenological LPBF model is numerically implemented via the finite element method within the program "NIsoS" developed by the authors based on the MOOSE framework Tonks et al. (2012). The parallel CPU computation is employed for each simulation batch containing multiple 3D finite element domains. The H-adaptive meshing scheme with error indicators on both T and ϕ (Fig. 1a$_3$) is also implemented to reduce the calculation consumption. Each domain has DOFs on the order of 100,000 for both nonlinear and auxiliary systems and is allotted with 48 processors and 2 GByte RAM per processor based on OpenMPI.

Each finite element domain in the simulation batch has a volume of $5000 \times 500 \times 550\ \ \mu\mathrm{m}^3$, containing a 50-$\mu$m-thick powder bed layer and a 500-μm-thick substrate layer made of the same materials as the powder, as shown in Fig. 1a$_1$. Except the bottom facet set with the Dirichlet boundary condition (BC), i.e.

$$T|_{\Gamma_{\mathrm{D}}} = T_0, \tag{16}$$

all the other facets are set with the combined BC of convection and radiation as

$$-k\nabla T|_{\Gamma_{\mathrm{C}}}\cdot\hat{\mathbf{n}} = h\left(T|_{\Gamma_{\mathrm{C}}} - T_0\right) + \varepsilon\sigma_{\mathrm{B}}\left(T|^4_{\Gamma_{\mathrm{C}}} - T_0^4\right) \tag{17}$$

with the convectivity h, Stefan-Boltzmann constant σ_{B}, the hemispherical emissivity ε, and the pre-heating (environmental) temperature T_0.

Quantities of constants above, as well as the thermal properties for SS316L particles and Argon atmosphere, are explicitly listed in Table 1.

Table 1
Thermal properties of industrial alloys used for the numerical simulations.

Properties	Units	Value	References
k_{ss}	J/(s m K)	20	Kim (1975)
c_{ss}	J/(kg K)	700	Kim (1975)
ρ_{ss}	kg/m^3	7900	Kim (1975)
k_{at}	J/(s m K)	~ 0.06	Hoshino et al. (1986)
$(\rho c)_{\mathrm{at}}$	J/(m^3 K)	717.6	Chase (1998)
h_{at}	J/(s m^2 K)	~ 100	
σ_{B}	J/(sm^3 K^4)	5.67×10^{-8}	
T_{M}	K	1723	Kim (1975)
T_0	K	353	
ε	–	0.3	Helte (1993)

4. Results and discussion

Fig. 2a illustrates the effective heat conductivity of the powder bed $k_{\mathrm{pb}}^{\mathrm{eff}}$ vs. packing density, obtained from the mentioned models and measurements on the free powders of steel by Luikov et al. (1968) and Abyzov et al. (2013), SS316L by Rombouts et al. (2005), SS304 by Agapiou and DeVries (1989), iron by Rombouts et al. (2005), copper by Rombouts et al. (2005), and aluminum Abyzov et al. (2013), also denoted correspondingly in Fig. 2a. As the experimental validation, multiple specimens consisting of single track with the dimensions of $30 \times 20 \times 7$ mm (Fig. 1b$_1$) are fabricated under four laser beam diameters, i.e. 66, 109, 152 and 196 μm, and distinct process parameters.

Taking the packing density utilized in this work (65.7%) as an example, it is obvious that Voigt model forms the physical upper bound of the $k_{\mathrm{pb}}^{\mathrm{eff}}$. In contrast, ZSS model presents a good coherence to the experimental measurements from the free powders. However, nonlinear regressions of the calibrated phenomenological simulation results using ZSS model show a relatively larger deviation from the allometric relation $b = C_L E_L^{0.5}$ (specifically, wider 95% confidence interval, hereinafter as CI$_{95\%}$) than ones using Voigt model at each D_l. This derivation becomes even larger with the rising of laser beam diameter D_l, implying a general better applicability of the Voigt model in this case. Considering the assumed microstructure behind each model, we thereby attribute this better applicability of the Voigt model to the possible formation of the lamina-like microstructure in the powder bed, which is possibly generated during the pre-heating stage of the LPBF. In other words, the model suitable for predicting $k_{\mathrm{pb}}^{\mathrm{eff}}$ of the free powders might be no longer applicable, demanding further investigations regarding homogenization of thermal properties on pre-heated powder bed during LPBF and detailed discussion according to effects of pre-heating to the microstructure and homogenized properties.

To further validate the allometric relation $b = C_L E_L^{0.5}$ with varying

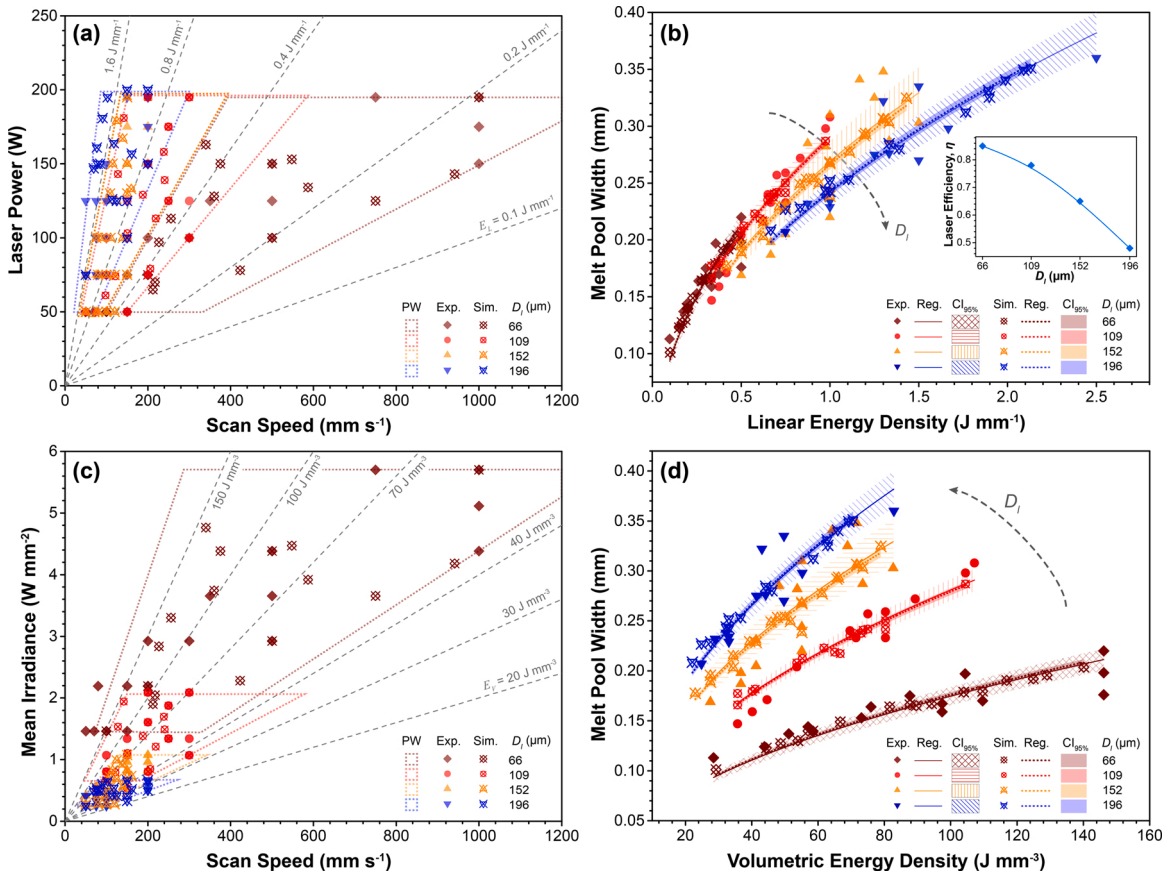

Fig. 3. (a) The process window (PW) represented by laser power and scan speed and (b) the corresponding regression of $b = C_L E_L^{0.5}$. Inset: calibrated laser efficiency η vs. laser beam diameter D_l. (c) The PW represented by laser mean irradiance and scan speed, and (d) the corresponding regression of $b = C_V E_V^{0.5}$.

laser beam diameter D_l, multiple set of process parameters, i.e. the laser power P and scan speed v, are sampled randomly (hereinafter as P-v set) within PWs of corresponding D_l for both experiments and simulations, as shown in Fig. 3a. Regressed curves and corresponding $CI_{95\%}$ are included in the Fig. 3b (calibrated $\eta(D_l)$ is shown in the inset, and the regression parameters are presented in Table 2). By comparing the regressed curves of the allometric relation, it shows that small changes in linear energy density cause large responses in the resulting melt pool width for the case $D_l = 66\,\mu$m. Increasing D_l leads to a monotonic decreasing in coefficient C_L of the tendency trend, resulting in reducing in melt pool width at the same E_L. Meanwhile, calibrated η drops along with the increase of E_L, demonstrating a reduction in effective absorptivity to the laser beam. One of the possible reason is due to the competition of enhanced laser scattering against the reduced mean irradiance when enlarging the beam spot under the experimental condition. On the one hand, enlarged laser beam can smooth the absorption fluctuation by covering more powders within the spot, reducing the effects from the variation in local powder packing, as spotted by Boley et al. (2017). On the other hand, enlarged laser beam can increase the scattering events of laser on the powder bed, including the ones that partially hit the non-fused powders, as visualized by Khairallah et al. (2020). With the reduction in the irradiance of the enlarged beam spot at the identical power (as shown in Fig. 1a$_4$), less laser penetration could be eventually deduced. Note this deduction should be made at the cases with relatively low laser power (holds also for parameters taken within the PW), i.e., no significant vaporization, as the enlarged laser beam in the high-power cases would result in the widening depressed melt pool, hosting more absorption events within it and thereby less dependence to the local powder packing, as stated by Khairallah et al. (2020). It also demonstrates that simple phenomenological simulations with calibrated $\eta(D_l)$ can well reproduce the proposed allometric relation, deducted from the experiments. Notably, the simulation results present a high correlation to the proposed allometric relation with less deviation, reflected by considerably narrowed $CI_{95\%}$ of that is completely enclosed by the experimental ones. Regression analysis shows that correlation coefficient $R^2 = 97.7\%$ for the simulated melt pool width with $D_l = 66$ μm, followed by 97.3% for $D_l = 109$ μm, 96.7% for $D_l = 152$ μm and 97.6% for $D_l = 196$ μm. As comparison, regression analysis on the experimental measured melt pool width presents correspondingly 71.2% for $D_l = 66$ μm, 92.7% for $D_l = 109$ μm, 68.7% for $D_l = 152$ μm and 81.7% for $D_l = 66$ μm.

In order to incorporate the influence from the laser beam diameter D_l, the other form of the allometric relation $b = C_V E_V^{0.5}$ as elaborated in Eq. (3b) with the volumetric energy density E_V is examined. Fig. 3c reveals that introducing the laser beam irradiance into the PW enables to

Table 2
Regression analysis of $b = C_L E_L^{0.5}$. Here σ represents the standard deviation, and R^2 represents the correlation coefficient.

	D_l(μm)	66	109	152	196
Exp.	C_L	0.299	0.291	0.269	0.242
	σ	0.007	0.005	0.008	0.005
	R^2	0.712	0.927	0.687	0.817
Sim.	C_L	0.301	0.289	0.266	0.242
	σ	0.002	0.002	0.002	0.002
	R^2	0.977	0.973	0.967	0.976

utilize the latter as boundaries for the PW, which is not the case for the linear energy density, cf. Fig. 3a. For the SS316L specimens investigated in this study, the reliable PW lies between beam irradiances I of 40 W mm^{-2} and 150 W mm^{-2}, making the mean irradiance I a more efficient parameter to characterize PWs and melt pool properties with process parameters. Introducing the volumetric energy density E_V further allows for better visualization of the significant influence of beam diameter and energy density on the width of the melt pool, as shown in Fig. 3d. It worth noting that the regression analysis does not show differences in both relations since they are linearly related, i.e., $C_V = C_L\sqrt{\pi}D_l/2$, proving the unity of the allometric relation and resultant scaling law in an LPBF system, disregarding the chosen type of characteristic energy density.

On the other hand, however, introducing the spot diameter D_l does not resemble a holistic description of the melt pool size in the dimensional state. As presented by Großmann et al. (2019) and Großmann et al. (2020), the derived scaling law works independently of the selected material, yet the effect from the beam-size-dependent laser efficiency $\eta(D_l)$, which has a significant influence on machine productivity as stressed by Metelkova et al. (2018), does not count. We would start this discussion from the effects of $\eta(D_l)$ on "shifting" scaling law by the adiabatic efficiency, H_{adi}. According to Trapp et al. (2017), the effective absorptivity is experimentally quantified by dividing the energy necessary to uniformly heat up the powder bed with the characteristic temperature distance $\Delta T = T_M - T_0$ by the obtained laser irradiance. Disregarding temperature-dependency on all thermal properties, it yields $\alpha^{eff} = V\rho cv\Delta T/lP$, where V and l are the volume and length of the heated-up region (the melt pool). Emphasizing again definition of H_{adi} (Eq. (2)) and the implementation of η inside the penetration profile of α^{eff} (14), one can further deduce the following relation $\alpha^{eff}[\eta(D_l)] \propto H_{adi}$ by approximating $V \propto b^2 l$ as the first-order approximation on melt pool depth elaborated in Section 2.1. This implies the potential relation between H_{adi} and beam-size-dependent laser attenuation. In this regard, effects from thermal efficiency characteristic H_{adi} and beam-size-dependent laser efficiency $\eta(D_l)$ can be collectively presented as the intercept shift with respect to the laser diameter change, as shown in Fig. 4a, where it clearly shows that the increasing D_l result in decreasing intercepts, reflecting the reduction in both thermal and laser efficiency.

Meanwhile, we could portray that $\eta(D_l)$ is involved by modifying the efficiency of the laser absorption, as clearly demonstrated in Fig. 3 where the laser beam diameter D_l alters the trend of allometric relation by significantly changing the η rather than the volumetric energy density. By recalling Eq. (12), we have the integral of laser-induced heat q over the whole simulation domain Ω as $\int_\Omega q = \eta(D_l)P$ and further declare its establishment also for the experimental measurements. On this ground, P_+ should be rescaled as ηP_+ with calibrated $\eta(D_l)$, representing physically the reduction of effective laser power due to variation in laser beam size. The scaling law is thereby reformulated as

$$\mathrm{Pe} = H_{adi}(\eta P_+)^{0.5}, \tag{18}$$

or in the deduced logarithmic form

$$\ln \mathrm{Pe} = \frac{1}{2}\ln(\eta P_+) + \ln\ H_{adi}. \tag{19}$$

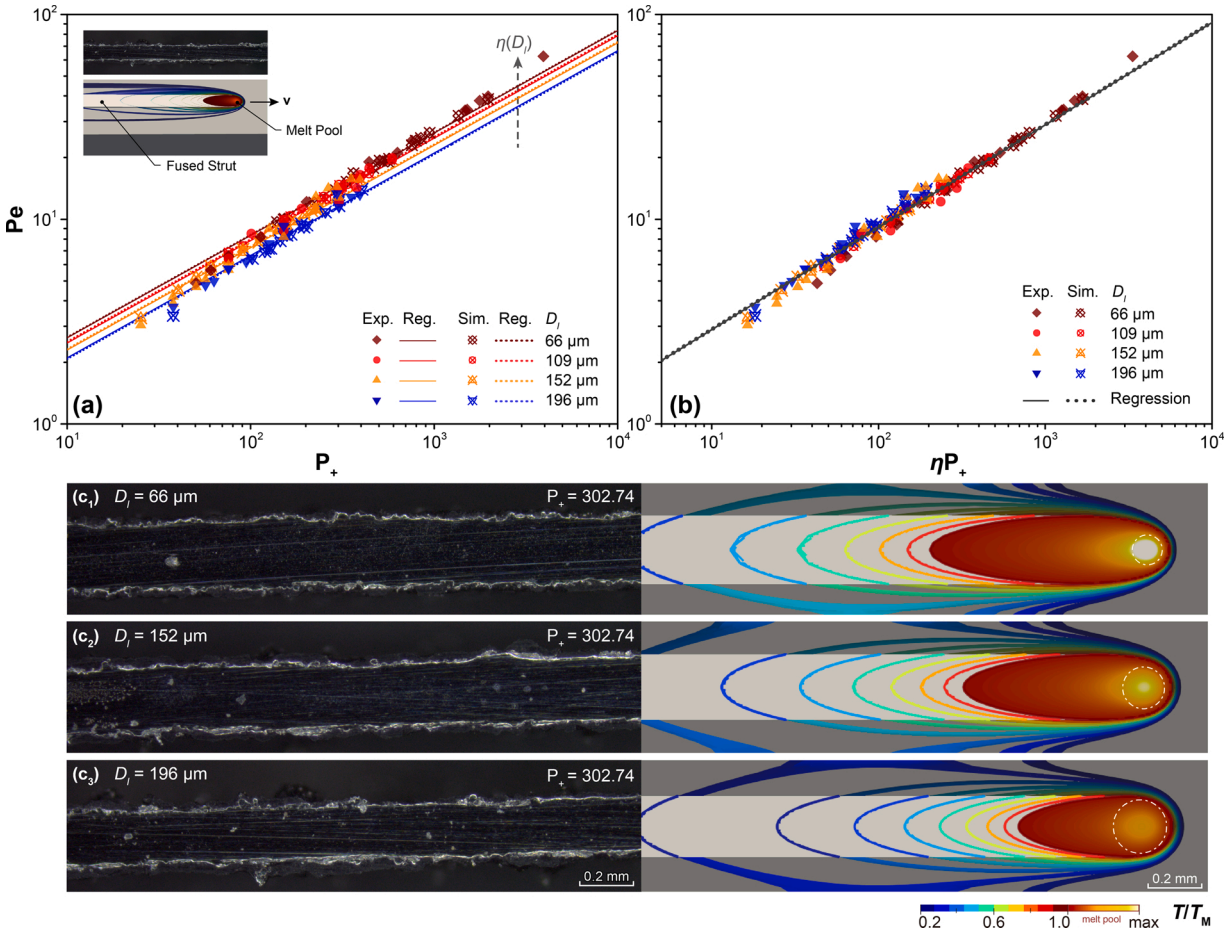

Fig. 4. Dimensionless allometric scaling law between Pe and P_+ (a) before and (b) after scaling w.r.t. calibrated laser efficiency η. (c_1)-(c_3) Experimental/numerical characterizations at chosen $P_+ = 302.74$.

In Fig. 4b it presents the regression of all experimental/numerical results to the sole scaling law as Eq. (19) with the correlation coefficient $R^2 = 97.8\%$ for experimental measurements and 99.3% for simulation results collectively, validating that $\eta(D_l)$ is an additional scaling factor in this physical system, and the scaling law Pe-ηP$_+$ is further independent to the beam size. It further demonstrates the potential relation between H_{adi} and $\eta(D_l)$ as $H_{adi}\eta^{0.5} = \text{const}$ from the sense that the interceptions generated in Fig. 4a due to $\ln H_{adi}$ is "shifted back" by $\frac{1}{2}\ln\eta$. Effects from such reduction in efficiency can also be characterized by the shrink of melt pool width and resultant strut thickness. In this sense, relatively smaller Pe is obtained at larger D_l for every chosen P_+, implying a smaller melt pool width. It is also experimentally and numerically spotted with good consistency as the one-by-one comparisons shown in Fig. 4c. To sum up briefly, the proposed scaling law is capable of being advanced with respect to the thermal and beam-size-dependent laser efficiency, thus resembles a beam and material independent physical characterization of the melt pool width and resultant strut thickness.

5. Conclusions

In this contribution we derived an improved dimensionless scaling law to correlate the melt pool width with material and process parameters in a beam-size independent fashion, which has been validated by both phenomenological simulations and experimental measurements under varying laser beam diameter. Two characteristic dimensionless numbers – Peclet number Pe and effective laser power P_+ have been correlated in a close form with a newly-defined dimensionless adiabatic energy efficiency H_{adi}, and rescaled by introducing a beam-size-dependent efficiency $\eta(D_l)$ to achieve the beam-size independence, i.e., $\text{Pe} = H_{adi}(\eta P_+)^{0.5}$.

This scaling law results in a largely enhanced freedom for process driven manufacturing in two directions: the melt pool width can be either scaled up in order to improve build rates significantly in the hatching region, or scaled down in the contour region to obtain a high surface quality of the manufactured components to reduce post processing effort. It can be further used to manufacture thin-walled micro-lattice architectures precisely, e.g. for medical implants, chromatography based substance separation, crash absorbers, or heat exchangers. Here, the smallest strut thickness obtained was 113 μm. On the next stage, this scaling law must be improved by further considering exposure types, such as point exposure, to determine the corresponding coefficients. Besides, the melt pool dynamics should be included such as temperature-dependent surface-tension gradients, which would enable the control of the underlying kinetics on the micro-second level and thus the reduction of the minimal strut thickness down to the order of magnitude of the powder diameter.

The presented method also offers an efficient framework for developing customized process parameters for both high productivity and precision for any given powder material and laser beam diameter. This enables real-time applications, such as melt pool geometry monitoring, defect and failure detection based, and compensatory process adjustment to improve the reliability and repeatability of the component's quality, readily associating with other methodologies like machine learning. Further, It would help building digital twins to predict, control, and adapt the process during manufacturing of large printed components with vastly reduced computational consumption (by more than two orders of magnitude as reported by Wei et al. (2021)). Future research should focus on providing more constitutive laws that include more relevant process parameters such as layer thickness to maximize the flexibility in process driven component design and to foster the utilization of digital twins for additive manufacturing.

Conflict of interest

The authors declare no conflict of interest.

Authors' contribution

Yangyiwei Yang: Methodology, Formal analysis, Software, Data curation, Writing – Original draft preparation. **Alexander Großmann:** Conceptualization, Resources, Verification, Data curation, Writing – Original draft preparation. **Patrick Kühn:** Formal analysis, Visualization, Investigation. **Jan Mölleney:** Investigation. **Lorenz Kropholler:** Investigation. **Christian Mittelstedt:** Supervision, Writing – Reviewing and Editing. **Bai-Xiang Xu:** Supervision, Writing – Reviewing and Editing.

Declaration of Competing Interest

The authors report no declarations of interest.

Acknowledgements

Y. Yang and B-.X. Xu acknowledges the financial support of the German Research Foundation (DFG) under the Collaborative Research Centre Transregio 270 (CRC-TRR 270, project number 405553726, sub-project A06), and the Research Training Groups 2561 (GRK 2561, project number 413956820, sub-project A4). The authors also greatly appreciate their access to the Lichtenberg High-Performance Computer, and the technique supports from the HHLR, Technische Universität Darmstadt.

Appendix A. Powder bed packing density estimation

Empirical equation w.r.t. polydispersity δ and skewness S from Ref. Desmond and Weeks (2014)

$$\psi = 0.634 + 0.0658\delta + 0.0857S\delta^2 \tag{A.1}$$

with ψ the volume fractional packing density of solid material. As for Gaussian-type size distribution $p(\widetilde{d}) = \frac{1}{\sqrt{2\pi}\widetilde{\sigma}} exp\frac{-(\widetilde{d}_i-1)^2}{2\widetilde{\sigma}^2}$ with the mean $\overline{d}$, the normalized diameter $\widetilde{d}_i = d_i/\overline{d}$ and normalized standard deviation $\widetilde{\sigma} = \sigma/\overline{d}$. We define $\Delta d = d_i - \overline{d}$, then according to the definitions of δ and S

$$\delta = \frac{\sqrt{\langle \Delta d^2 \rangle}}{\langle d \rangle} = \widetilde{\sigma}, \quad S = \frac{\langle \Delta d^3 \rangle}{\langle \Delta d^2 \rangle^{\frac{3}{2}}} = 0. \tag{A.2}$$

Meanwhile, via assuming Gaussian-type size distribution of the particles, we can also resolve σ and $\overline{d}$ from the characteristic diameters d_{10}, d_{50} and d_{90} as

$$\sigma \approx \frac{d_{90} - d_{10}}{2.564}, \quad \overline{d} = d_{50}. \tag{A.3}$$

Therefore the volume fractional porosity φ of a powder bed with Gaussian-type size distribution can be approximated according to the characteristic diameters as

$$\varphi = 1 - \psi = 0.366 - \frac{0.0257}{2.564}\left(\frac{d_{90} - d_{10}}{d_{50}}\right) \tag{A.4}$$

In this work, A SS316L powder bed with $d_{10} = 16.12\ \mu$m, $d_{50} = 28.78\ \mu$m and $d_{90} = 42.23\ \mu$m was employed. Assuming the Gaussian-type size distribution, the packing density and porosity were calculated as $\psi = 65.7\%$ and $\varphi = 34.3\%$.

Appendix B. Dimensional analysis

Table A1 presents the quantities of interest w.r.t. four fundamental dimensions of a stable LPBF system. According to the Buckingham Π-theorem Buckingham (1914), the whole system can be described by two dimensionless numbers, each of which is also the combination of those dimensional quantities, i.e. $\prod_i \widehat{q}_i^{a_i^j}$ with $\widehat{q}_i = b,\ P,\ v,\ k,\ (\rho c)$ and ΔT. The indice vector $\mathbf{a}_j = [a_i^j]^{\mathrm{T}}$ $(i = 1,2,3,4,5,6;\ j = 1,2)$, containing indice of corresponding quantities, is determined by finding the kernel of matrix $\mathbf{A}$ forming from Table A1, i.e.

$$\mathbf{A}\mathbf{a}_j = 0 \quad \text{with} \quad \mathbf{A} = \begin{bmatrix} 1 & 2 & 1 & 1 & -1 & 0 \\ 0 & 1 & 0 & 1 & 1 & 0 \\ 0 & -3 & -1 & -3 & -2 & 0 \\ 0 & 0 & 0 & -1 & -1 & 1 \end{bmatrix} \tag{B.1}$$

There a number of solutions to Eq. (B.1). Based on the quantities of interest P and b, two linear independent solutions were chosen:

$$\mathbf{a}_1 = \begin{bmatrix} 1 \\ 0 \\ 1 \\ -1 \\ 1 \\ 0 \end{bmatrix} \quad \text{and} \quad \mathbf{a}_2 = \begin{bmatrix} 0 \\ 1 \\ 1 \\ -2 \\ 1 \\ -1 \end{bmatrix} \tag{B.2}$$

Using Eq. (B.1) in combination with Eq. (B.2) two dimensionless numbers Pe and P_+ can be constructed as,

$$\mathrm{Pe} = \frac{bv\rho c}{k} \quad \text{and} \quad \mathrm{P}_+ = \frac{Pv\rho c}{k^2 \Delta T}, \tag{B.3}$$

where Pe fits the definition of the Peclet number, which is used to characterize the relative scale of advective to diffusive transport of the quantity of interest (when scan speed v has the same scale of the melt flow speed).

Following the same procedure in Eqs. (B.1)–(B.2), a single dimensionless parameter $\mathrm{H}_{\mathrm{adi}}$ can be further concluded on the adiabatic melting/resolidification system (i.e. a further simplified dimension system as Table A2 with effect from thermal conduction vanished) as we explained in the content

$$\mathrm{H}_{\mathrm{adi}} = \frac{b^2 v \rho c \Delta T}{P}. \tag{B.4}$$

Table A1
Dimensional table of process parameters and material properties in a [LMTΘ]-system.

	b	P	v	k	ρc	ΔT
L	1	2	1	1	− 1	0
M	0	1	0	1	1	0
T	0	− 3	− 1	− 3	− 2	0
Θ	0	0	0	− 1	− 1	1

Table A2
Dimensional table of process parameters and material properties in a [LMTΘ]-system under the assumption of adiabatic melting and resolidification.

	b	P	v	ρc	ΔT
L	1	2	1	− 1	0
M	0	1	0	1	0
T	0	− 3	− 1	− 2	0
Θ	0	0	0	− 1	1

References

Abyzov, A.M., Goryunov, A.V., Shakhov, F.M., 2013. Effective thermal conductivity of disperse materials. I. compliance of common models with experimental data. Int. J. Heat Mass Transf. 67, 752–767.

Agapiou, J.S., DeVries, M.F., 1989. An experimental determination of the thermal conductivity of a 304l stainless steel powder metallurgy material. J. Heat Transf. 111, 281–286.

Arısoy, Y.M., Criales, L.E., Özel, T., 2019. Modeling and simulation of thermal field and solidification in laser powder bed fusion of nickel alloy IN625. Opt. Laser Technol. 109, 278–292.

Barenblatt, G., 1996. Scaling, Self-similarity, and Intermediate Asymptotics: Dimensional Analysis and Intermediate Asymptotics. Cambridge University Press, Cambridge.

Bauereiß, A., Scharowsky, T., Körner, C., 2014. Defect generation and propagation mechanism during additive manufacturing by selective beam melting. J. Mater. Process. Technol. 214, 2522–2528.

Bidare, P., Bitharas, I., Ward, R., Attallah, M., Moore, A., 2018. Laser powder bed fusion in high-pressure atmospheres. Acta Mater. 142, 107–120.

Boley, C.D., Khairallah, S.A., Rubenchik, A.M., 2017. Calculation of laser absorption by metal powders in additive manufacturing. Addit. Manuf. Handb. Prod. Dev. Def. Ind. 54, 507–517.

Bridgman, P., 1922. Dimensional analysis. Yale University Press, New Haven.

Buckingham, E., 1914. On physically similar systems; illustrations of the use of dimensional equations. Phys. Rev. 4, 345–376.

Chase Jr., M.W., 1998. NIST-JANAF thermochemical tables. J. Phys. Chem. Ref. Data Monogr. 9.

Curtarolo, S., Hart, G.L., Nardelli, M.B., Mingo, N., Sanvito, S., Levy, O., 2013. The high-throughput highway to computational materials design. Nat. Mater. 12, 191–201.

Denlinger, E.R., Jagdale, V., Srinivasan, G., El-Wardany, T., Michaleris, P., 2016. Thermal modeling of Inconel 718 processed with powder bed fusion and experimental validation using in situ measurements. Addit. Manuf. 11, 7–15.

Desmond, K.W., Weeks, E.R., 2014. Influence of particle size distribution on random close packing of spheres. Phys. Rev. E 90, 022204.

Fabbro, R., Dal, M., Peyre, P., Coste, F., Schneider, M., Gunenthiram, V., 2018. Analysis and possible estimation of keyhole depths evolution, using laser operating parameters and material properties. J. Laser Appl. 30, 032410.

Goossens, L., van Hooreweder, B., 2021. A virtual sensing approach for monitoring melt-pool dimensions using high speed coaxial imaging during laser powder bed fusion of metals. Addit. Manuf. 40, 101923.

Großmann, A., Felger, J., Frölich, T., Gosmann, J., Mittelstedt, C., 2019. Melt pool controlled laser powder bed fusion for customised low-density lattice structures. Mater. Des. 181, 108054.

Großmann, A., Mölleney, J., Frölich, T., Merschroth, H., Felger, J., Weigold, M., Sielaff, A., Mittelstedt, C., 2020. Dimensionless process development for lattice structure design in laser powder bed fusion. Mater. Des. 194.

Guo, C., Li, S., Shi, S., Li, X., Hu, X., Zhu, Q., Ward, R.M., 2020. Effect of processing parameters on surface roughness, porosity and cracking of as-built IN738LC parts fabricated by laser powder bed fusion. J. Mater. Process. Technol. 285, 116788.

Gusarov, A., Yadroitsev, I., Bertrand, P., Smurov, I., 2009. Model of radiation and heat transfer in laser-powder interaction zone at selective laser melting. J. Heat Transf. 131, 072101.

Hann, D., Iammi, J., Folkes, J., 2011. A simple methodology for predicting laser-weld properties from material and laser parameters. J. Phys. D: Appl. Phys. 44, 445401.

Helte, A., 1993. Radiative and conductive heat transfer in porous media: estimation of the efective thermal conductivity. J. Appl. Phys. 73, 7167–7173.

Herzog, D., Seyda, V., Wycisk, E., Emmelmann, C., 2016. Additive manufacturing of metals. Acta Mater. 117, 371–392.

Hoshino, T., Mito, K., Nagashima, A., Miyata, M., 1986. Determination of the thermal conductivity of argon and nitrogen over a wide temperature range through data evaluation and shock-tube experiments. Int. J. Thermophys. 7, 647–662.

Hussein, A., Hao, L., Yan, C., Everson, R., 2013. Finite element simulation of the temperature and stress fields in single layers built without-support in selective laser melting. Mater. Des. 52, 638–647.

ISO, 2005. Lasers and laser-related equipment-Test methods for laser beam widths, divergence angles and beam propagation ratios-Part 1: Stigmatic and simple astigmatic beams. Standard ISO 11146-1: 2005 (E).

Khairallah, S., Anderson, A., Rubenchik, A., King, W., 2016. Laser powder-bed fusion additive manufacturing: Physics of complex melt flow and formation mechanisms of pores, spatter, and denudation zones. Acta Mater. 108, 36–45.

Khairallah, S., Martin, A., Lee, J., Guss, G., Calta, N., Hammons, J., Nielsen, M., Chaput, K., Schwalbach, E., Shah, M., 2020. Controlling interdependent meso-nanosecond dynamics and defect generation in metal 3d printing. Science 368, 660–665.

Khairallah, S.A., Anderson, A., 2014. Mesoscopic simulation model of selective laser melting of stainless steel powder. J. Mater. Process. Technol. 214, 2627–2636.

Kim, C.S., 1975. Thermophysical properties of stainless steels. Technical Report ANL-75-55. Argonne National Lab, IL, USA.

King, W., Barth, H., Castillo, V., Gallegos, G., Gibbs, J., Hahn, D., Kamath, C., Rubenchik, A., 2014. Observation of keyhole-mode laser melting in laser powder-bed fusion additive manufacturing. J. Mater. Process. Technol. 214, 2915–2925.

King, W.E., Anderson, A.T., Ferencz, R.M., Hodge, N.E., Kamath, C., Khairallah, S.A., Rubenchik, A.M., 2015. Laser powder bed fusion additive manufacturing of metals; physics, computational, and materials challenges. Appl. Phys. Rev. 2, 041304.

Kirkpatrick, S., 1973. Percolation and conduction. Rev. Mod. Phys. 45, 574.

Leung, C., Marussi, S., Atwood, R., Towrie, M., Withers, P., Lee, P., 2018. In situ x-ray imaging of defect and molten pool dynamics in laser additive manufacturing. Nat. Commun. 9.

Li, Y., Gu, D., 2014. Parametric analysis of thermal behavior during selective laser melting additive manufacturing of aluminum alloy powder. Mater. Des. 63, 856–867.

Luikov, A., Shashkov, A., Vasiliev, L., Fraiman, Y.E., 1968. Thermal conductivity of porous systems. Int. J. Heat Mass Transf. 11, 117–140.

Markl, M., Körner, C., 2016. Multiscale modeling of powder bed-based additive manufacturing. Annu. Rev. Mater. Res. 46, 93–123.

Maxwell, J., 1954. A Treatise on Electricity and Magnetism. New York, Dover Publications.

Metelkova, J., Kinds, Y., Kempen, K., Formanoir, C., Witvrouw, A., van Hooreweeder, B., 2018. On the influence of laser defocusing in selective laser melting of 316l. Addit. Manuf. 23, 161–169.

Meza, L., Das, S., Greer, J., 2014. Strong, lightweight, and recoverable three-dimensional ceramic nanolattices. Science 345, 1322–1326.

Mukerjee, T., Manvatkar, V., De, A., DebRoy, T., 2017. Dimensionless numbers in additive manufacturing. J. Appl. Phys. 121, 064904.

Oliveira, J., Santos, T., Miranda, R., 2020. Revisiting fundamental welding concepts to improve additive manufacturing: From theory to practice. Prog. Mater. Sci. 107.

Panwisawas, C., Tang, Y., Reed, R., 2020. Metal 3d printing as a disruptive technology for superalloys. Nat. Commun. 11, 2327.

Pelz, P., Vergé, A., 2014. Validated biomechanical model for efeciency and speed of rowing. J. Biomech. 47, 3415–3422.

Popovich, V., Borisov, E., Popovich, A., VS, S., Masaylo, D., Alzina, L., 2017. Functionally graded inconel 718 processed by additive manufacturing: Crystallographic texture, anisotropy of microstructure and mechanical properties. Mater. Des. 114, 441–449.

Purcell, E., 1977. Life at low reynolds number. Am. J. Phys. 45, 3–11.

Rai, R., Elmer, J., Palmer, T., DebRoy, T., 2007. Heat transfer and fluid flow during keyhole mode laser welding of tantalum, ti-6al-4v, 304l stainless steel and vanadium. J. Phys. D: Appl. Phys. 40, 5753–5766.

Roberts, I.A., Wang, C., Esterlein, R., Stanford, M., Mynors, D., 2009. A three-dimensional finite element analysis of the temperature field during laser melting of metal powders in additive layer manufacturing (english). Int. J. Mach. Tools Manuf. 49, 916–923.

Robinson, J., Ashton, I., Fox, P., Jones, E., Sutcliffe, C., 2018. Determination of the effect of scan strategy on residual stress in laser powder bed fusion additive manufacturing. Addit. Manuf. 23, 13–24.

Romano, J., Ladani, L., Razmi, J., Sadowski, M., 2015. Temperature distribution and melt geometry in laser and electron-beam melting processes – a comparison among common materials. Addit. Manuf. 8, 1–11.

Rombouts, M., Froyen, L., Gusarov, A., Bentefour, E.H., Glorieux, C., 2005. Photopyroelectric measurement of thermal conductivity of metallic powders. J. Appl. Phys. 97, 024905.

Rubenchik, A., King, W., Wu, S., 2018. Scaling laws for the additive manufacturing. J. Mater. Process. Technol. 257, 234–243.

Rubenchik, A., Wu, S., Mitchell, S., Golosker, I., LeBlanc, M., Peterson, N., 2015. Direct measurements of temperature-dependent laser absorptivity of metal powders. Appl. Opt. 54, 7230–7233.

Sih, S.S., 1996. The thermal and optical properties of powders in selective laser sintering. University of Texas at Austin, Ph.D. thesis.

Smil, V., 2013. Making the Modern World: Materials and Dematerialization, 1st ed. Wiley, Weinheim.

Souza, J., Großmann, A., Mittelstedt, C., 2018. Micromechanical analysis of the effective properties of lattice structures in additive manufacturing. Addit. Manuf. 23, 53–69.

Thümmler, F., Oberacker, R., et al., 1993. An Introduction to Powder Metallurgy, vol. 490. The University Press, Great Britain.

Tonks, M.R., Gaston, D., Millett, P.C., Andrs, D., Talbot, P., 2012. An object-oriented finite element framework for multiphysics phase field simulations. Comput. Mater. Sci. 51, 20–29.

Trapp, J., Rubenchik, A.M., Guss, G., Matthews, M.J., 2017. In situ absorptivity measurements of metallic powders during laser powder-bed fusion additive manufacturing. Appl. Mater. Today 9, 341–349.

Velasco-Hogan, A., Xu, J., Meyers, M., 2018. Additive manufacturing as a method to design and optimize bioinspired structures. Adv. Mater. 30, 1800940.

Wang, Y.M., Voisin, T., McKeown, J.T., Ye, J., Calta, N.P., Li, Z., Zeng, Z., Zhang, Y., Chen, W., Roehling, T.T., Ott, R.T., Santala, M.K., Depond, P.J., Matthews, M.J., Hamza, A.V., Zhu, T., 2018. Additively manufactured hierarchical stainless steels with high strength and ductility. Nat. Mater. 17, 63–70.

Wei, H., Mukherjee, T., Zhang, W., Zuback, J., Knapp, G., De, A., DebRoy, T., 2021. Mechanistic models for additive manufacturing of metallic components. Prog. Mater. Sci. 116, 100703.

West, G., Brown, J., Enquist, B., 1997. A general model for the origin of allometric scaling laws in biology. Science 276, 122–126.

Yang, Y., Kühn, P., Yi, M., Egger, H., Xu, B.X., 2020. Non-isothermal phase-field modeling of heat–melt–microstructure-coupled processes during powder bed fusion. JOM 72, 1719–1733.

Yang, Y., Ragnvaldsen, O., Bai, Y., Yi, M., Xu, B.X., 2019. 3d non-isothermal phase-field simulation of microstructure evolution during selective laser sintering. NPJ Comput. Mater. 5, 1–12.

Yi, M., Xu, B.X., Gutfleisch, O., 2019. Computational study on microstructure evolution and magnetic property of laser additively manufactured magnetic materials. Comput. Mech. 64, 917–935.